IEEE Access
Multidisciplinary | Rapid Review | Open Access Journal

Received November 5, 2018, accepted January 10, 2019, date of publication January 31, 2019, date of current version February 20, 2019.

Digital Object Identifier 10.1109/ACCESS.2019.2895620

Electrical and Thermal Characterization of 3D Printed Thermoplastic Parts With Embedded Wires for High Current-Carrying Applications

KAZI MD MASUM BILLAH[1,2], JOSE L. CORONEL[1,2], Jr., MICHAEL C. HALBIG[3], RYAN B. WICKER[1,2], AND DAVID ESPALIN[1]

[1]W.M. Keck Center for 3D Innovation, The University of Texas at El Paso, El Paso, TX 79968, USA
[2]Department of Mechanical Engineering, The University of Texas at El Paso, El Paso, TX 79968, USA
[3]NASA Glenn Research Center, Cleveland, OH 44135, USA

Corresponding author: Kazi Md Masum Billah (kbillah@miners.utep.edu)

This work was supported in part by the National Aeronautics and Space Administration under Grant NNC17CA02C, in part by the MacIntosh Murchison Chair I in Engineering Endowment, and in part by the Air Force Research Laboratory, under Grant FA8650-12-2-7230.

ABSTRACT Fabrication of parts exhibiting multi-functionality has recently been complemented by hybrid polymer extrusion additive manufacturing in combination with wire embedding technology. While much mechanical characterization has been performed on parts produced with fused deposition modeling, limited characterization has been performed when combined electrical and thermal loads are applied to 3D printed multi-material parts. As such, this paper describes the design, fabrication, and testing of 3D printed thermoplastic coupons containing embedded copper wires that carried current. An automated fabrication process was used employing a hybrid additive manufacturing machine that dispensed polycarbonate thermoplastic and embedded bare copper wires. Testing included AC and DC hipot testing as well as thermal testing on as-fabricated and heat treated coupons to determine the effect of porosity in the substrate. The heat-treated parts contained reduced amounts of porosity, as corroborated through scanning electron microscopy, which led to a 50 % increased breakdown strength and 30 to 40 % increased heat dissipation capabilities. The results of this paper are describing a set of design protocol that can be used as a guideline for 3D printed embedded electronics to predict the electrical and thermal behavior.

INDEX TERMS Multi^{3D} additive manufacturing, hybrid additive manufacturing, wire embedding, hipot testing, heat treatment, heat dissipation.

I. INTRODUCTION

Interest in additive manufacturing for producing end-use parts continues to rise as essentially all industries explore possible applications. For example, General Electric made a bold promise to produce over 100,000 turbine engine parts produced by additive manufacturing for the LEAP and GE9x engines by 2020 [1]. In the hearing aid industry, 3D printing is responsible for $\sim$ 99% of all custom in-the-ear hearing aid shells [2], [3]. Additive manufacturing (AM), more popularly referred to as 3D printing, has matured beyond fabrication of common structures into fabrication of multi-functional parts, which possess electrical or actuation functionality, for example, in addition to mechanical or structural functionality [4]–[6]. The focus on multifunctionality has led to the direct inclusion of electronics during fabrication of a 3D printed part, often referred to as 3D printed electronics. This area has gained interest because of the potential to simplify supply chains, and the opportunities to integrate electronic systems, including sensors, into a printed part [5]. Prior research in electronic component integration via hybrid AM (i.e., integration of a complementary manufacturing technology with AM) produced functional parts through two AM technologies, vat photopolymerization and material extrusion [5]–[7]. In the case of vat photopolymerization, direct-write micro-dispensing technologies were integrated to selectively dispense conductive inks for interconnection purposes [5], [6] to fabricate a magnetic sensor, a temperature sensor, and a gaming die [8], [10], [11]. Challenges limiting

The associate editor coordinating the review of this manuscript and approving it for publication was Bora Onat.

this approach included the high bulk resistivity of the conductive ink traces and the need to process conductive inks on plastic substrates, which limited curing and sintering temperatures because of the substrate's thermal properties [10], [11].

In pursuit of improved functionality, hybrid approaches have also been developed for material extrusion, to include the embedding of solid conductors within thermoplastic substrates [12]–[15] resulting in radiating elements for antennas [16], [17] and interconnect for embedded circuitry [18], [19]. Improved performance in interconnections was obtained through the use of solid conductive wires instead of conductive inks wherein exhibited lower resistivity ($1.78 \times 10^{-8}\ \Omega \cdot$ m for copper at 20°C vs. $11.8 \times 10^{-8} \Omega \cdot$ m for silver-based ink CB028), higher current carrying capacity and lower cost (0.05 USD for 1g Cu wire vs. $2 \sim 20$ USD for 1g silver ink). Though solid conductors were deemed superior to inks for current carrying applications, integration of embedded wires in AM parts lacks the extensive research necessary to quantify the benefits and drawbacks. Multi-process AM systems exclusively adapted to produce 3D printed electronics, require characterization of their fabricated parts to develop new methods for enhancing their reliability and efficiency. Specifically, the understanding of electrical and thermal characterization will aid in developing guidelines for designing 3D printed electronics, with the aim of fabricating compact electromechanical devices using hybrid AM.

3D printed material extrusion parts inherently possess challenges with porosity, dimensional accuracy, and voids. Several factors such as resolution, temperature of the printing environment, and thermal gradient within the rasters are responsible for undesirable print qualities [20]. In the context of 3D printed electronics, the possible failure modes increase due to the introduction of additional electric and thermal stresses. Challenges arise because of the mismatch in coefficient of thermal expansion (CTE), and in turn, the adhesion between the thermoplastic substrate and the solid conductors. Continuous accumulation of heat generated by embedded electrical components will result from the low thermal conductivity of thermoplastics (0.18 to 0.22 W/m · K). Additionally, lack of adhesion between disparate materials (thermoplastic and conductor), results in increased porosity and reduced thermal conductivity. Increased porosity results in decreased overall thermal conductivity as the conductivity of air is ∼0.02 W/m K. This is due to the fact that air has a lower thermal conductivity (0.02 W/m · K) than thermoplastics. The relationship between porosity and thermal conductivity can be corroborated using Voigt's rule. In the case of embedded electronics, the increased porosity, inability to effectively dissipate heat, and the mismatch in CTE, lead to distortion of the fabricated part. Subsequently, thermal deformation causes mechanical stress on the substrate material, leading to failure during long term operation [21]. Repair of fully encapsulated and embedded wires (and electrical components when present) is often not possible because access to each is prohibited by the encapsulating thermoplastic. However, this encapsulating feature can also serve to reduce tampering and reverse engineering, which can be beneficial in certain application. In addition, the inclusion of access panels can be included into the geometrical design to allow access for some maintenance and probing.

The presence of high current carrying wires exacerbates the detrimental effects of porosity and voids. Electrical stress is generated by the conductor, ultimately leading to dielectric breakdown, leakage current (partial discharge), and electrical treeing in the insulation material (substrate) [22]. While failure of the insulation material in conventional devices, axial flux stators for example, can be attributed to voids during manufacturing or wear of insulating material due to unintended wire movement/vibration, thermal distortion occurs due to ohmic losses and the thermal contact resistance located at the encapsulated conductor and interconnections [23]. In general, the presence of voids within an insulation material of electrical components causes failure due to decreased breakdown strength. Breakdown strength, also known as high electrical potential (hipot), is the ability of an insulating material to withstand a sudden rise of voltage. This parameter is essential for medium voltage applications, such as electric motors (300∼1000V), to ensure the reliability of the manufactured components. In general, there exists the possibility of extensive damage to parts containing electrical components due to repeated thermal, mechanical, and electrical stresses [23].

To the authors knowledge, the effect of porosity on breakdown strength, thermal conductivity, and heat dissipation in Fused Deposition Modeling (FDM) was not previously reported. Therefore, a vacant area of research exists for determining the implication of porosity on the electrical and thermal behavior of thermoplastic substrates. As interest grows in multi-material, multi-functional electronic devices, data captured from characterizing the interaction between embedded conductors and thermoplastics can be used in the design of 3D printed electronics. The presented research aims at addressing the need for characterization of embedded conductors to accurately simulate their effects on thermoplastic substrates. Coupons were fabricated with commercially available materials; polycarbonate (PC) substrate via material extrusion AM, and bare copper wires for the conductors. Data gathered from coupon level testing serves as a benchmark for the future development of a model that would potentially be used to design optimal 3D printed electronics that accommodate for the detrimental effects of voltage on the substrate. Deeper understanding of the interface between conductor and substrate could lead to the fabrication of power electronics such as stators, inductors for wireless chargers, or even embedded transformers.

II. EXPERIMENT

A. FABRICATION

For testing and characterization purposes, three sample sets of wire embedded coupons, each containing ten specimens, were fabricated. Each sample set had either one, two, or three

wires embedded within each specimen. A linear wire embedding configuration was used to fabricate coupons. It was anticipated the encapsulation of more than one wire can produce a substantial amount of data to design a fabrication protocol of 3D printed electronics. Therefore, the fabrication of coupons were extended from one wire to three wires. Of the ten specimens within each group, five were tested in an as-fabricated condition while the other five specimens were heat treated before testing. The heat treatment consisted of placing the specimens in an oven for two hours to reach the steady state condition. The oven temperature was set at 165 °C, which was above the glass transition temperature of PC (161 °C) [24], to promote polymer chain mobility and reduction of voids while limiting temperature induced dimensional changes, which were observed to be more pronounced above 165 °C. Note that the scope of heat treatment of FDM part is limited to embedded wires only. In case of embedded electronic component, exposure to heat treatments can be detrimental to the component's functionality. Therefore, selection of the electronic components must consider the heat treatment. As an example, if the heat treatment is at or below 150 °C, traditional silicon integrated circuits can be used. However, if the heat treatment is above 150 °C, Silicon On Insulation (SOI) complementary metal-oxide semiconductor (CMOS) technology can be used since the components can operate continuously at temperatures up to 225 °C for at least five years.

The 3D printing was accomplished by using a Multi^{3D} manufacturing system briefly described here. The interested reader can find a further description of the Multi^{3D} manufacturing system in [21], [25], and [26]. The Multi^{3D} machine consisted of an industrial MH50 six-axis robot (Yaskawa Motoman, Miamisburg, OH, USA) with several manufacturing stations within its reach including two production-grade Fortus 400mc Fused Deposition Modeling (FDM) machines (Stratasys, Eden Prairie, MN, USA) and a LC 3024 CNC machine (Techno CNC Systems, Ronkonkoma, NY, USA) capable of using multiple custom tools, including a wire embedding tool, machining spindle, pick-and-place end-effectors, and foil application tool as described in [26] and [27].

The manufacturing approach used by the Multi^{3D} system was such that thermoplastic material was dispensed by an FDM machine onto a portable build platform, which was transported by the six-axis robot to the other manufacturing stations. At any point during fabrication, the workpiece could have been returned to the original FDM machine to deposit more thermoplastic material onto the partially fabricated part. For this work, the Multi^{3D} system was used to deposit polycarbonate (PC) (Stratasys, Eden Prarie, MN, USA) and embed a series of 26 AWG ($Ø = 0.405$ mm) bare copper wires (Arcor Electronics, Niles, IL, USA) in an automated fashion. The full encapsulation of copper wire within the PC material was accomplished by 1) dispensing PC material to produce a substrate, 2) transferring, via the six-axis robot, the workpiece to the CNC machine where wire was automatically embedded using a custom cartridge heating wire embedding tool, and 3) transferring the workpiece back to the FDM printer to deposit PC onto the substrate and fully encapsulate the wire. Figure 1 shows computer-aided design (CAD) representations for each of the three sample groups. The coupon dimensions were 25 × 15 × 2.5 mm, and coupons were printed in the XYZ orientation [27] The thickness of the coupon was chosen small (2.5 mm) to determine breakdown strength during high electrical stress across a short distance of insulating material. The 3D printing layer thickness was set at 0.254 mm (0.010 inch). The coupon was fabricated by stacking six PC layers before embedding the copper wire, which was embedded within the sixth PC layer and occupied approximately half the thickness of the fifth PC layer. The designed lateral distance (center-to-center) between wires in the two-wire and three-wire coupons was 2 mm. In Figure 1 detailed dimensions of the embedded wires within the three-wire substrate are shown. To evaluate the accuracy of the fabrication process, 3D printed specimens were cut into two pieces using a Techcut 5^{TM}Precision High Speed Saw (Allied High Tech Products Inc., Rancho Dominguez, CA, USA) and subsequently inspected using a TM 1000 table top optical microscope (Hitachi High Technologies Europe GmbH, Germany) and a Smartscope Flash 250 (Optical Gaging Products Inc., Rochester, NY, USA).

B. TESTING

Three characterization techniques were used: hipot testing using AC and DC, thermal testing, and cross-sectional micrograph analysis.

1) HIPOT TESTING

The results of a comprehensive survey were presented in IEEE Electrical Insulation Conference in Montreal, Canada 2009 [28] stating that 90% of power electronics experts suggested the use of AC hipot testing for as-fabricated components (e.g., stators) of electrical machines. AC testing was preferred because of its ability to detects defects, availability of AC supply (most common in domestic and industrial application), and short testing time (maximum 10 seconds as compared to 60 seconds for DC hipot testing). Since one of the goals of this research was to determine the insulation robustness of 3D electronics, both AC and DC hipot testing were performed through the use of a HiPot-3870 Tester with a device under testing (DUT) enclosure (Associated Research Inc., Lake Forest, IL, USA). Figure 2 presents the experimental schematic used for hipot testing. The wire embedded coupons were placed and tested inside the DUT enclosure while the conductive copper wire was connected to the high voltage electrode and the insulating polycarbonate was connected to the low voltage electrode of the hipot tester. According to IEEE Std-4-1995, the AC hipot testing voltage was chosen by the following equation [29]:

$$V_{AC\_Test} = \left(2 \times V_{Operational} + 1000\right) \tag{1}$$

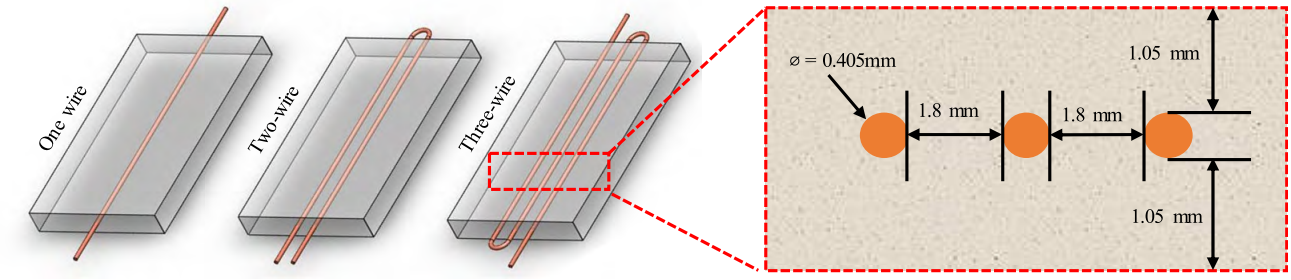

FIGURE 1. CAD for fabricated coupon with expected cross-sectional dimensions.

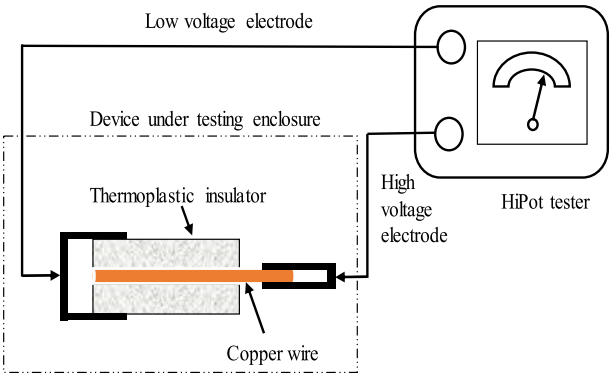

FIGURE 2. Schematic of high potential(hipot)test setup.

In the case of DC hipot testing, the test voltage was chosen using the following equation:

$$V_{DC\_Test} = \left(2 \times V_{Operational} + 1000\right) \times 1.7 \qquad (2)$$

where "Test" and "Operational" are the expected and end-use operating voltage, respectively. During AC hipot test, the considered $V_{\text{Operational}}$ was 2,000 V; the total voltage ramp time was 0.1 s; and the frequency was 60 Hz. Based on these values, V_{AC_Test} varied from 0 to 5 kV within 0.1 s. The total time of each test was 10 s in two stages: the first stage was 0.1 s for ramp up to the maximum voltage 5 kV, the second stage was 9.9 s to maintain the steady state condition at 5 kV voltage.

The DC test was performed similarly to the AC test by considering $V_{\text{Operational}}$ as 970 V, which resulted in a V_{DC_Test} of 5 kV. In the DC test, the total voltage ramp was 5 s and total dwell time was 1 minute. Both AC and DC tests were performed by supplying 5000 μA current into the conductive part. To evaluate the consistency of the results, each of the test specimens was tested five times within a 10 minute interval. The time interval was chosen to allow power cycling of the hipot tester in such a manner that there was no residual voltage or current within the test specimen.

2) THERMAL TESTING

The purpose of this work was to quantify the effect of porosity on surface temperature increase. However, the transcendant goal was the creation of a design protocol for 3D electronics that will predict their thermal behaviour. A temperature analysis was performed on the three different groups of coupons in the following ways:

- analytical solution using a) classical heat transfer theory or b) a superposition method,
- numerical solution using commercially-available software, and
- empirical measurements using thermocouples.

In the analytical approach, classical heat transfer is considered to be laborious to determine the ohmic losses and convective heat transfer coefficient in each case while the superposition method only needs the single wire parameters (ohmic loss and heat transfer coefficient) to predict the thermal behavior in multiple wires.

Of interest was the steady state temperature of the embedded wire due to the supplied current and the corresponding temperature of the exterior insulator surface. The analytical and numerical solution analyses were performed to assess their applicability in future designs containing embedded wires, and therefore facilitating and expediting the design of such parts.

To analytically determine the surface temperature of the specimen and embedded wire, a steady-state cylindrical coordinate system was considered with an imaginary boundary (dotted circle as shown in Figure 3.) around the wire. For the overlapping regions of the two- and three-wire specimens, superposition was used to capture the conductive heat transfer contribution. Using this approach, the following analytical expressions were arrived at that included a multiplier (n) for representing superposition and the number of conduction sources:

$$\dot{Q} = \frac{(T_c - T_\infty)}{(n \times R_{conduction} + R_{convection})}\,[W] \qquad (3)$$

$$R_{conduction} = \frac{\ln\left(\frac{r_2}{r_1}\right)}{2\pi Kl}\left[\frac{^\circ C}{W}\right] \qquad (4)$$

$$R_{Convection} = \frac{1}{hA} = \frac{1}{h\,(2\pi r_2)\,l}\left[\frac{^\circ C}{W}\right] \qquad (5)$$

where T_c is the copper wire surface temperature, T_∞ is room temperature (assumed 24 °C), r_1 is the conductor radius,

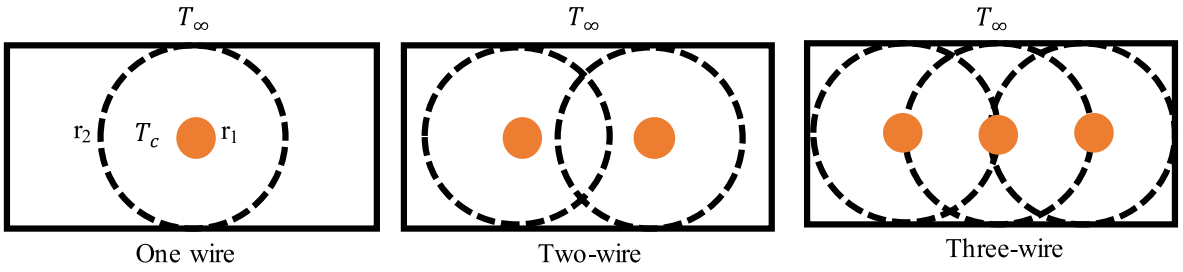

FIGURE 3. Proposed heat transfer model for multiple stationary heat sources within rectangular block.

r_2 is the radius of the imaginary boundary within the thermoplastic, l is the length of conductor, k is the effective thermal conductivity, h is the convective heat transfer coefficient, $R_{convective}$ is the equivalent resistance due to the convective heat transfer, and $R_{conduction}$ is the conductive resistance due to the conduction through the thermoplastic (PC). Note that the superposition method still required a classical approach to assume the heat transfer coefficient.

In the classical approach the temperature of the substrate (T_s) and conductor surface (T_c) was calculated using the following equations:

$$\dot{Q} = \frac{(T_s - T_\infty)}{R_{convection}}\,[W] \tag{6}$$

$$R_{Convection} = \frac{1}{hlw}\left[\frac{^\circ C}{W}\right] \tag{7}$$

$$\dot{Q} = \frac{(T_c - T_\infty)}{(R_{conduction} + R_{convection})}\,[W] \tag{8}$$

$$R_{Conduction} = \frac{t}{klw}\left[\frac{^\circ C}{W}\right] \tag{9}$$

where w is the width of the specimen, and t is the thickness of the specimen. Since the classical approach is based on temperature dependent convective coefficient, the Nusselt (Nu) and Raleigh (Ra) number were calculated using the empirical film temperature.

For the numerical solution approach, the steady state surface temperature was determined by considering the Joule heating within the embedded wire and the thermal conductivity through the printed thermoplastic. The numerical simulation was performed using the ANSYS steady state thermal module (ANSYS, Inc., Canonsburg, PA) using the following boundary conditions: convective heat transfer coefficient (h) of 12, 15, and 15.27 W/m^2/°C (based on the classical approach which determined the Rayleigh number and Nusselt number using the film temperature property table) for all six sides of the one-, two-, and three-wire thermoplastic coupon respectively, an effective conductive heat transfer coefficient (k) of 0.18 W/m/K (based on the use of the Voigt model when considering k for PC equal to 0.20 W/m/K, k for air equal to 0.02 W/m/K, and empirical volume fraction for printed PC equal to 0.9).

After predicting the temperatures (using equation sets 3-5 and 6-9 as well as ANSYS simulations), an empirical method was used to conduct thermal testing using the Joule heating principle. The Joule heating effect was created by passing current through the embedded copper wire. According to the Joule's heating law, the following mathematical expression described the heating effect:

$$\dot{Q} = I^2 R\,[W] \tag{10}$$

where $\dot{Q}$ is the heating effect in watts (W), I is the current in amps (A) flowing through the conductive element, and R is the resistance in ohm (Ω) of the current-carrying conductor. Joule heating was generated in the embedded copper wire (Ø = 0.405 mm) within PC by supplying current (5 A) from a DC power supply (BK PRECISION 9115, B&K Precision Corporation, Yorba Linda, CA, USA). In Figure 4, the thermal test schematic using Joule heating effect is shown. Two K-type thermocouples were placed on the top and bottom surface of the specimen to collect the temperature change due to Joule heating. Data were acquired using a NI – cDAQ 9426 thermal data acquisition (DAQ) device (National Instruments, Austin, TX) linked to a computer. Data were acquired every second for a span of two hours.

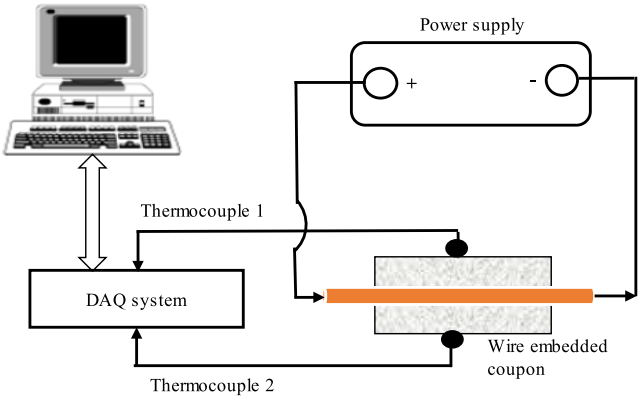

FIGURE 4. Schematic of thermal testing of wire embedded coupon.

It is important to mention that thermal testing of the wire embedded coupon was performed in two steps. First, the test was carried out before the heat treatment of the coupon (as-fabricated), and the second test was performed after the heat treatment. For each test specimen, three separate tests were performed at different times to verify the repeatability of the experimental data.

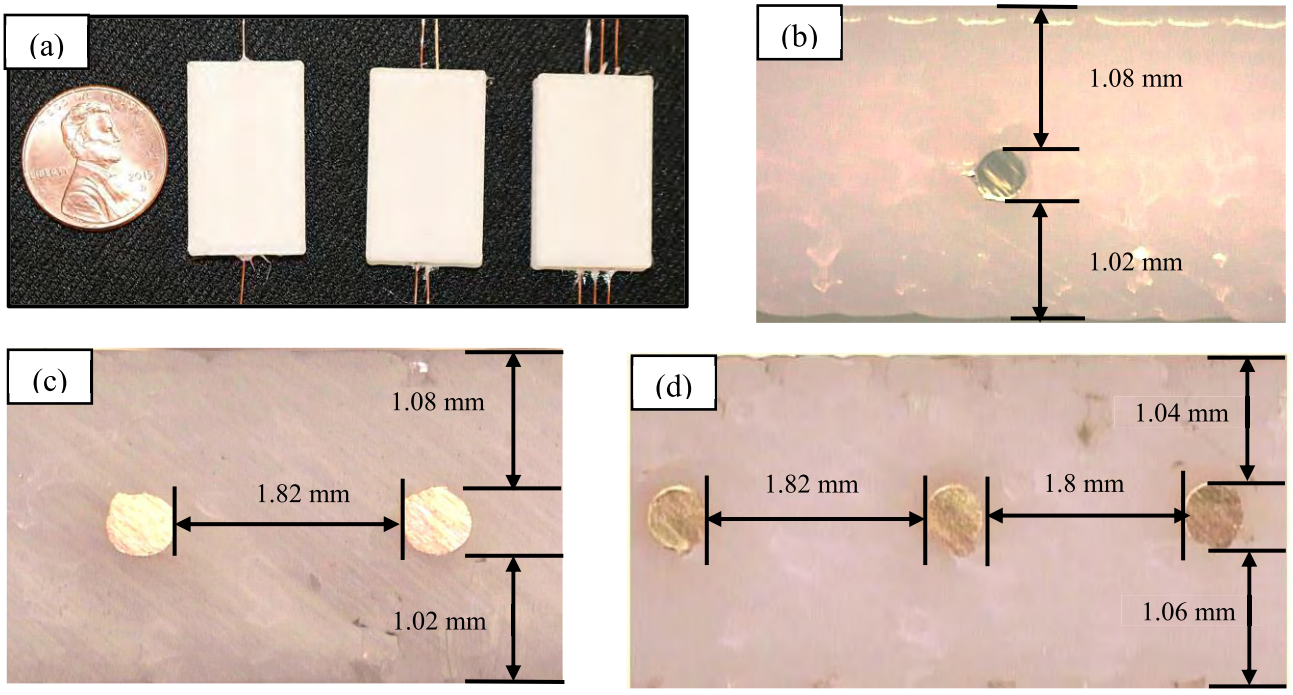

FIGURE 5. (a) fabricated coupons with US penny for scale (b) cross-sectional dimensions of one-wire coupon, (c) two-wire coupon, and (d) three-wire coupon.

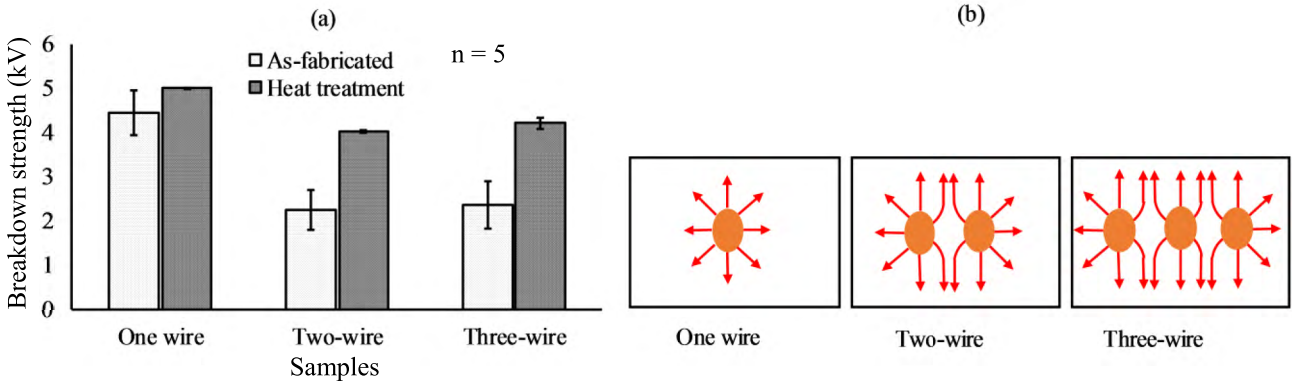

FIGURE 6. (a) AC hipottesting resultsof three groups of wire embedded couponand (b) visual representation of electric field within coupon.

III. RESULT AND DISCUSSION

A. CROSS-SECTIONAL IMAGES FOR COUPONS WITH EMBEDDED WIRES

In Figure 5(a), 3D printed and wire embedded coupons are shown. The cross-section images in Figure 5(b)-(d) were taken to measure the dimensional accuracy of the embedded wire placement. The maximum error (when comparing against the intended CAD dimension) of embedded wire placement was found as 2.8 % for one-wire and two-wire specimens, and 1.1 % for three-wire specimens.

B. AC AND DC HIPOT TESTING

AC hipot testing was performed to determine the coupons ability to withstand low and medium voltages. Note that it was not the goal to determine the dielectric strength of the PC material, which has been reported by the manufacturer as 3.2 kV/mm [30], rather the objective was to determine the electrical insulating capability of the coupons in a simulated real-life application. Figure 6(a) shows the average breakdown strength (AC hipot testing) from five measurements for each group before and after heat treatment. The measured range of breakdown strength for as-fabricated one-, two-, and three-wire specimens were 4 to 4.8 kV, 1.98 to 2.6 kV, and 2 to 2.8 kV, respectively. Note that the specimen thickness (2.5 mm) was constant for all specimens. One could expect that breakdown strength of coupons would decrease with increasing number of wires, which was the case when comparing the one-wire and two-wire specimens, however,

TABLE 1. Analytical versus simulated wire temperature of one-, two-, and three-wire coupon.

Number of Wires	*Length of embedded wire (mm)*	*Analytical temperature of wire (°C)*		*Simulated temperature of wire (°C)*
		Classical	*Superposition*	
1	40	56	58	57
2	75	69	67	69
3	85	76	77	76

the comparisons of the two-wire and three-wire specimens does not agree with the expectation. In the linear wire configuration used, the breakdown strength is not expected to increase if additional wires are included in the same configuration. The electric field around the wires remains the same if the distance between wire-to-wire remains the same. Breakdown strength is expected to decrease only when newly added wires are placed in close proximity to already-existing wires such that their electrical fields interact.

The cartoon diagram in Figure 6(b) of the electric field for the embedded wire illustrates the electric field distribution. When multiple wires were embedded in close proximity, the net electric field strength was higher than the single wire electric field because of individual wire electric field contributions. The relatively higher net electric field strength caused the two-wire and three-wire specimens to exhibit a decreased, yet similar, breakdown strength. Hence, the breakdown strength of the two-wire and three-wire specimens were approximately 50 % lower than the one-wire samples. Furthermore, inserting components into the printed part will likely affect the breakdown strength, given that the components will either create a pathway or obstruct the electric fields, as determined by the component's dielectric properties relative to the printed substrate. It should be stated that the embedding of electrical components has been previously demonstrated [16], [25] but not tested in regards to breakdown strength.

After carrying out the heat treatment, the breakdown strength of each group specimen was increased due to the reduction of voids within the printed PC material. Among the five tests, four of the one-wire specimen's breakdown strength was above 5 kV. Hence, the standard deviation (represented by the error bars in Figure 6) was small and almost unnoticeable in the graph. In the case of the two- and three-wire specimen, average breakdown strength was 4 to 4.03 kV and 4.15 to 4.3 kV, respectively. During DC hipot testing, all the specimens from the three sample groups passed (i.e., did not breakdown) when subjected to 5 kV in both the heat-treated and as-fabricated condition.

C. THERMAL TESTING OF HEAT-TREATED AND AS-FABRICATED SPECIMENS

The effect of porosity on the surface temperature caused by the embedded, current-carrying wires was quantified by conducting thermal testing before and after heat treating the printed thermoplastic. The analytical and ANSYS-simulated wire temperatures of embedded wires as a result of Joule heating are listed in Table 1. Note that, the analytical and simulated solutions are in good agreement. While the embedded wire and surface temperatures were determined in both analytical and numerical approach, only the PC surface temperature was measured empirically.

The thermoplastic surface temperature results (simulated and empirical) are reported in Figure 7. In the steady state condition, the substrate and conductor surface temperature of one-wire specimens were simulated as 51°C and 57°C, respectively, in Figure 7(a). The empirical surface temperature for the same as-fabricated specimen set was measured at 38°C. As expected, the heat-treated specimens produced a higher steady state surface temperature (51°C) – an increase of 34 % when compared to the one-wire as-fabricated specimens as shown in Figure 7(b). Also, the analytical temperature (classical) of the embedded wire and substrate surface were plotted to have the reference temperature of the empirical value. While the heat-treated surface temperature was in close agreement with the simulated temperatures, the as-fabricated surfaces were substantially lower. The mismatch was attributed to the inherent porosity of printed parts, which had an effect on the heat transfer coefficient.

In case of two-wire specimens, as shown in Figure 7(c), the simulated substrate surface temperature was 64 °C and was in close agreement to the measured surface temperature (66 °C) of specimens with heat treatment. The heat dissipation was increased by 34 % (49 °C for the as-fabricated specimens increased to 66 °C) after the heat treatment operation of the two-wire coupons as shown in Figure 7(d). Since the two-wire specimens had more supplied power, it was expected that the surface temperature would be higher when compared to the one-wire specimens (as-fabricated: 38 °C for one-wire vs. 49 °C for two-wire).

Lastly, the three-wire heat-treated specimens showed an increase in substrate surface temperatures of 26 % with respect to the as-fabricated specimen. The empirical steady-state surface temperature was 71 °C whereas the simulated temperature was 70 °C. The important finding for the three-wire specimen results was the agreement of analytical and simulated temperature of the solid conductor surface. This agreement also indicated that the superposition that accounted for the conductive heat transfer part in the analytical equation was valid and applicable for multiple stationary heat sources in a solid block substrate.

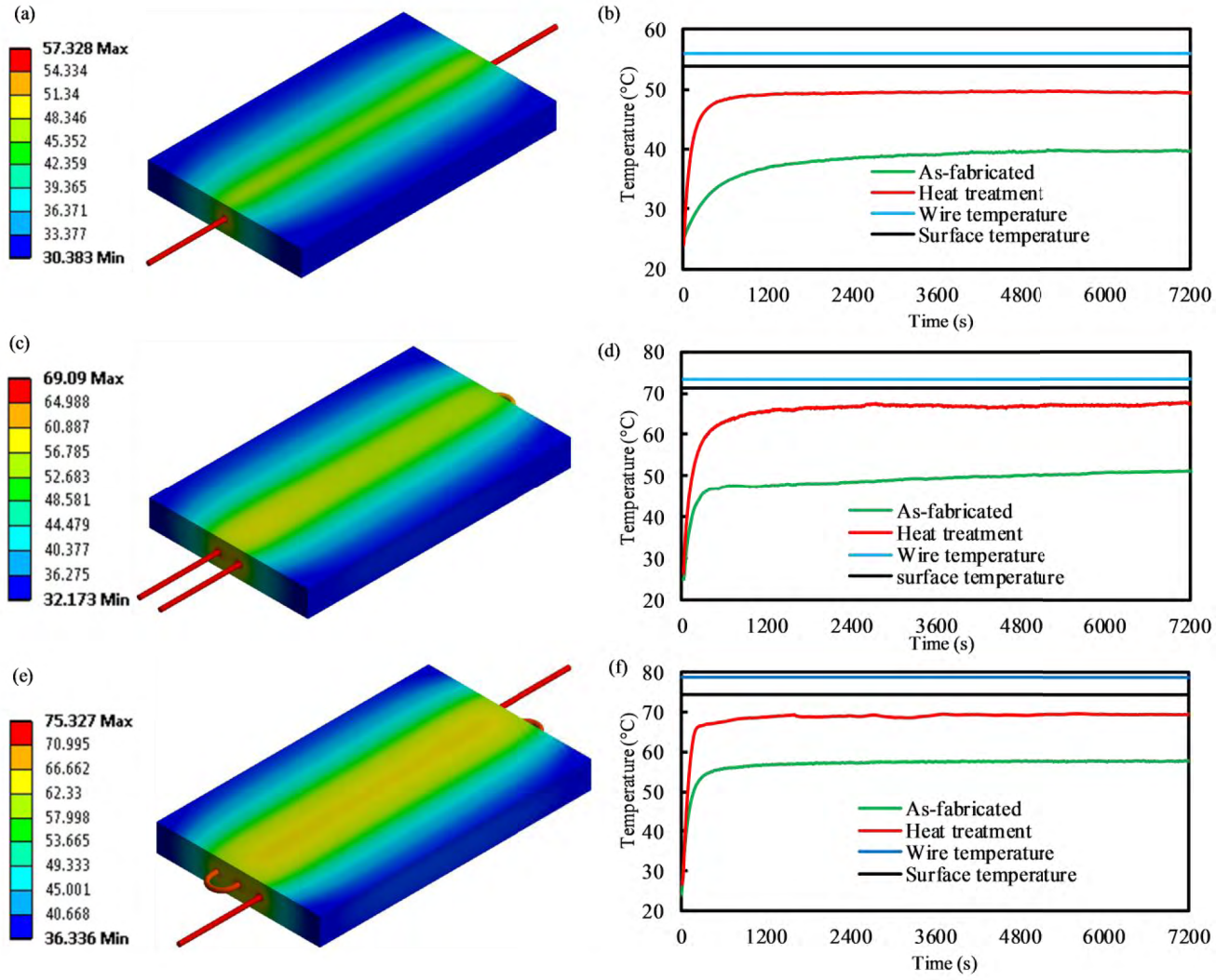

FIGURE 7. Simulated temperature contour plots for (a) one-wire, (c) two-wire, and (e) three-wire coupons. Experimental temperature profile for (b) one-wire, (d) two-wire, and (f) three-wire coupon. The steady state temperature as determined by the classical analytical method is also plotted.

In each group, there was a substantial temperature increase when comparing the as-fabricated and heat-treated specimens. Therefore, the heat treatment of 3D printed parts can be performed to reduce porosity and therefore increase the thermal conductivity. Porosity reduction increases the heat conductivity because air has a lower thermal conductivity (0.02 W/m · K) compared to the bulk PC's thermal conductivity (bulk 0.22 W/m · K and the effective thermal conductivity of PC was 0.18 W/m · K based on 0.9 PC volume fraction).

SEM images of heat-treated and as-fabricated 3D printed specimens revealed reductions in porosity. Thermal testing on heat treated and as-fabricated specimen confirmed that the presence of porosity reduced the heat dissipation whereas the heat-treated specimen exhibited higher heat conduction due to less porosity. In Figure 8, the difference in porosity between the as-fabricated and heat-treated specimens is noticeable. It was obvious that due to the expansion of raster at elevated temperature (165 °C during heat treatment), voids within the parts are reduced. Therefore, the bulk PC (or expanded raster) contributed the higher heat dissipation from the embedded wire to the environment.

D. DIMENSIONAL CHANGE

It is well understood that heat treatments on 3D printed polymer substrates will improve performance by significantly reducing porosity. However, it should be noted that heat treatment may result in negligible dimensional changes to the substrate. Torres *et al.* [31] suggested low levels (i.e., temperatures) of heat treatment to improve the strength of FDM parts while preserving ductility and reliability. The article, however, did not disclose the exact temperature for the ABS and PLA materials. For this work, the dimensional changes due to heat treatment for three set of specimens containing embedded wire are shown in Figure 9. The horizontal axis of the graph lists the dimension characteristic of

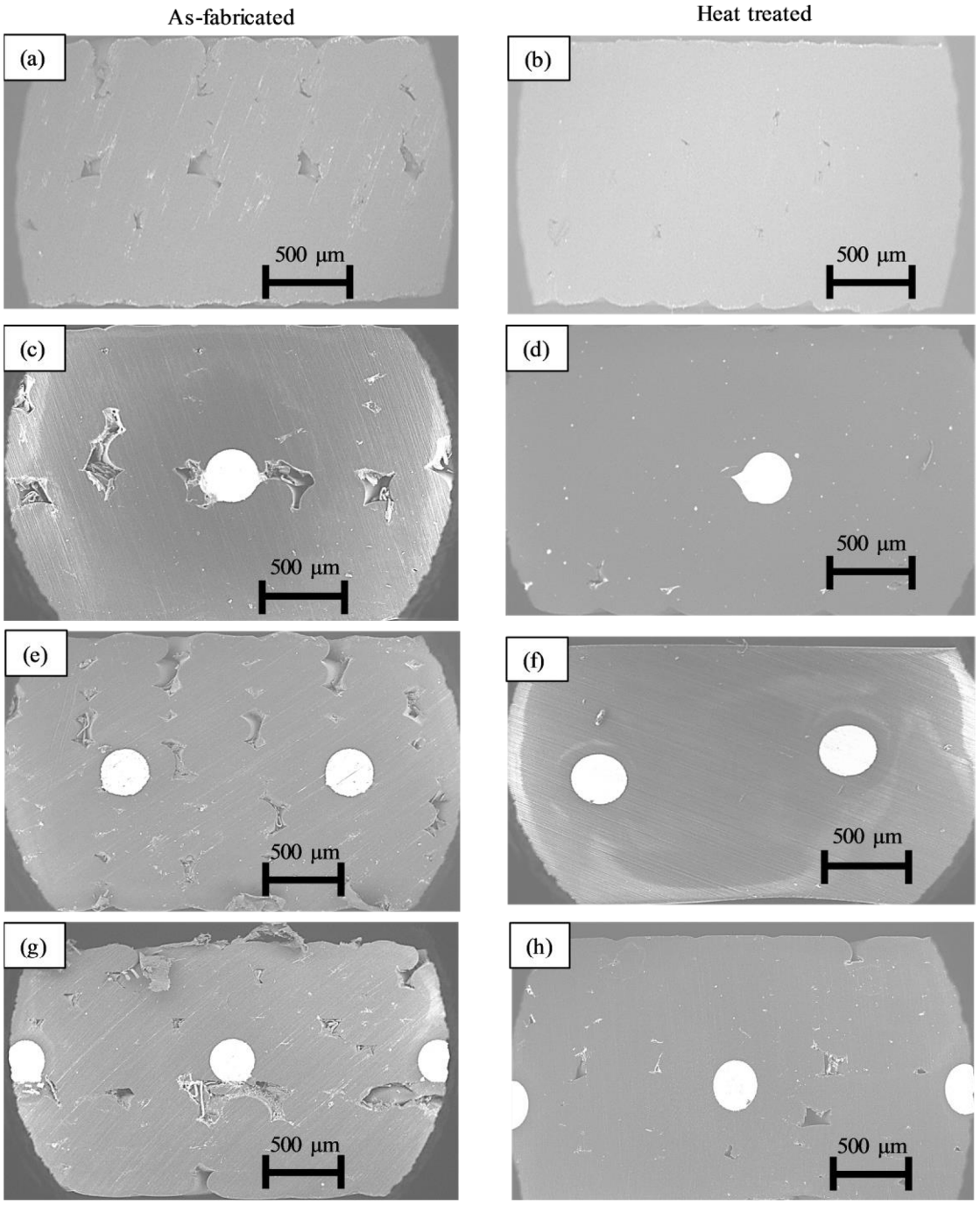

FIGURE 8. SEM image of cross sectionedas-fabricated specimen with (a) no wire, (c) one-wire, (e) two-wire,(g) three-wire and after heat treatment (b) nowire, (d) one-wire, (f) two-wire, and (h) three-wire.

the specimens and the vertical axis presents the dimensional change where positive changes indicate an increase in dimensions. In general, the difference between heat-treated and as-fabricated dimensions for all features increased due to the heat treatment. The largest change was noted in width, which was 0.17 mm (1.14 % increase when compared to the as-fabricated specimens). The length change was 0.15 mm (0.82 % increase when compared to the as-fabricated specimens) and thickness was 0.092 mm (1.90 % increase when compared to the as-fabricated specimens). In other words, due to the heat-treatment, the length and width were reduced to 0.13 mm and 0.12 mm, respectively. Also, it was expected that the reduction of the length and width due to the heat-treatment would have increased the thickness of the specimen, and this was corroborated by the measurements.

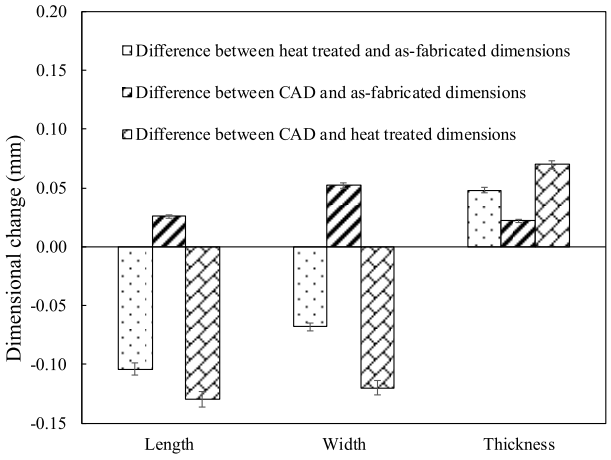

FIGURE 9. Mean dimensional changes due to the heat treatment of coupons containing embedded wires.

IV. SUMMARY AND CONCLUSION

This paper reported electrical and thermal characterization data addressing a knowledge gap for material extrusion 3D printed parts containing embedded current-carrying copper wires. In addition, this research was able to quantify the effect of reduced porosity, via a heat treatment, on breakdown strength and thermal properties. The breakdown strength testing using AC high electrical potential stress of as-fabricated parts showed that an initial increase of wires from one-wire to two-wires reduced the breakdown strength by approximately 50%, but the breakdown strength remained essentially the same when comparing two-wire and three-wire specimens because of the equivalent electric field interaction between adjacent wires. Testing of heat treated parts found that the increase in average breakdown strength and reduced standard deviations were attributed to the reduced porosity yielded by the heat treatment. In addition, a design approach for 3D printed wire-containing thermoplastics, akin to printed wiring boards, was identified to scrutinize temperature distributions. The recommended design protocol consists of using a superposition approach for an expedited initial design phase followed by a more accurate numerical simulation approach for the final design stage. The initial superposition approach is recommended since the convective heat transfer coefficient can be considered independent of temperature with minimal accuracy drawbacks. On the other hand, the numerical simulation approach requires that the convective heat transfer coefficient be determined for each design iteration, and therefore is only recommended for the final design stage. Through experimentation, it was determined that the presence of porosity within the PC substrate had an effect on the heat transferred from the embedded, heat generating wire to the external surface of the plastic. This was quantified in the case for example of the three-wire coupons where substrate temperature increased from 56°C to 71°C after reducing porosity by heat treatment.

In conclusion, electrical and thermal characterization data captured in this work can be utilized by manufacturers in AM community during the design, production and validation of 3D printed electrical devices where embedded wires are required to carry relatively high currents. Although this manuscript was focused on studying the breakdown strength and thermal dissipation of embedded wires in printed test specimens, a few thoughts are offered in regards to process qualification. Given that the fabrication process was executed in an automated fashion, it is feasible to introduce a flying probe tester (or similar machine) to inspect and qualify the fabricated parts. This testing can be performed at any specific layer similar to what is being proposed for wire embedding. The complexity of the part and embedded circuit may, in some cases, require the inclusion of access features so that embedded wires/components can be tested. In future, authors are envisioned to embed multiple layers of wire to investigate the compatibility and structural reliability along with this research work.

ACKNOWLEDGEMENT

The authors would like to thank the fabrication and characterization presented conducted at The University of Texas at El Paso (UTEP) within the W.M. Keck Center for 3D Innovation (Keck Center) using equipment developed via a previously funded effort through the National Center for Defense Manufacturing and Machining under the America Makes Program entitled '3D Printing Multifunctionality: Additive Manufacturing for Aerospace Applications' (Project #4030). Partial project support was provided by the Mr. and Mrs. MacIntosh Murchison Chair I in Engineering at UTEP (Ryan Wicker). The authors acknowledge the contribution of Carlos Acosta, Lluvia Herrera, Sol Barraza, and Leonardo Gutierrez for their assistance and support during experimentation.

The views and conclusions contained herein are those of the authors and should not be interpreted as necessarily representing the official policies or endorsements, either expressed or implied, of Air Force Research Laboratory or the U.S. Government. The U.S. Government is authorized to reproduce and distribute reprints for Governmental purposes notwithstanding any copyright notation thereon. This work was conducted at the W. M. Keck Center for 3D Innovation, The University of Texas at El Paso.

REFERENCES

[1] B. P. Conner *et al.*, "Making sense of 3-D printing: Creating a map of additive manufacturing products and services," *Additive Manuf.*, vols. 1–4, pp. 64–76, Oct. 2014.

[2] C.-Y. Liaw and M. Guvendiren, "Current and emerging applications of 3D printing in medicine," *Biofabrication*, vol. 9, no. 2, Jun. 2017, Art. no. 024102.

[3] C. G. Sandström, "The non-disruptive emergence of an ecosystem for 3D printing—Insights from the hearing aid industry's transition 1989–2008," *Technol. Forecasting Social Change*, vol. 102, pp. 160–168, Jan. 2016.

[4] J. T. Muth *et al.*, "Embedded 3D printing of strain sensors within highly stretchable elastomers," *Adv. Mater.*, vol. 26, no. 36, pp. 6307–6312, Sep. 2014.

[5] H. Ota *et al.*, "Application of 3D printing for smart objects with embedded electronic sensors and systems," *Adv. Mater. Technol.*, vol. 1, no. 1, Apr. 2016, Art. no. 1600013.

[6] M. Saari, B. Cox, E. Richer, P. S. Krueger, and A. L. Cohen, "Fiber encapsulation additive manufacturing: An enabling technology for 3D printing of electromechanical devices and robotic components," *3D Printing Additive Manuf.*, vol. 2, no. 1, pp. 32–39, 2015.
[7] C. Gutierrez *et al.*, "CubeSat fabrication through additive manufacturing and micro-dispensing," in *Proc. Int. Symp. Microelectron.*, vol. 1, Jan. 2011, pp. 1021–1027.
[8] E. MacDonald *et al.*, "3D printing for the rapid prototyping of structural electronics," *IEEE Access*, vol. 2, pp. 234–242, 2014.
[9] D. Espalin, D. W. Muse, E. MacDonald, and R. B. Wicker, "3D Printing multifunctionality: Structures with electronics," *Int. J. Adv. Manuf. Technol.*, vol. 72, nos. 5–8, pp. 963–978, May 2014.
[10] A. J. Lopes, E. MacDonald, and R. B. Wicker, "Integrating stereolithography and direct print technologies for 3D structural electronics fabrication," *Rapid Prototyping J.*, vol. 18, no. 2, pp. 129–143, 2012.
[11] D. W. Muse, R. Wicker, E. MacDonald, R. Salas, and F. Medina, "Electronic gaming die," U.S. Patent 9 908 037, Mar. 6, 2018.
[12] K. B. Perez and C. B. Williams, "Combining additive manufacturing and direct write for integrated electronics—A review," in *Proc. 24th Int. Solid Freeform Fabr. Symp. Additive Manuf. Conf. (SFF)*, Aug. 2013, pp. 962–979.
[13] D. A. Roberson, R. B. Wicker, L. E. Murr, K. Church, and E. MacDonald, "Microstructural and process characterization of conductive traces printed from Ag particulate inks," *Materials*, vol. 4, no. 6, pp. 963–979, May 2011.
[14] D. Espalin, D. Marquez, A. Fernandez, C. Kim, E. MacDonald, and R. Wicker, "Method and apparatus for wire handling and embedding on and within 3D printed parts," U.S. Patent 15 244 061, Mar. 2, 2017.
[15] D. Espalin, R. Wicker, A. Fernandez, J. Ramirez, and J. Motta, "Wire embedding system with a curved delivery path," U.S. Patent US20180070453, Mar. 8, 2018.
[16] C. Bailey *et al.*, "Augmenting computer-aided design software with multi-functional capabilities to automate multi-process additive manufacturing," *IEEE Access*, vol. 6, pp. 1985–1994, 2018.
[17] E. MacDonald *et al.*, "Fabricating patch antennas within complex dielectric structures through multi-process 3D printing," *J. Manuf. Processes*, vol. 34, pp. 197–203, Aug. 2018.
[18] C. Shemelya *et al.*, "Encapsulated copper wire and copper mesh capacitive sensing for 3-D printing applications," *IEEE Sensors J.*, vol. 15, no. 2, pp. 1280–1286, Feb. 2015.
[19] C. Shemelya *et al.*, "3D printed capacitive sensors," in *Proc. IEEE Sensors*, Nov. 2013, pp. 1–4.
[20] M. S. Hossain, D. Espalin, J. Ramos, M. Perez, and R. Wicker, "Improved mechanical properties of fused deposition modeling-manufactured parts through build parameter modifications," *J. Manuf. Sci. Eng.*, vol. 136, no. 6, Oct. 2014, Art. no. 061002.
[21] S. Ambriz *et al.*, "Material handling and registration for an additive manufacturing-based hybrid system," *J. Manuf. Syst.*, vol. 45, pp. 17–27, Oct. 2017.
[22] K. C. Agrawal, "Winding insulation and its maintenance," in *Industrial Power Engineering Handbook*. Woburn, MA, USA: Elsevier, 2001, pp. 9-219–9-229.
[23] K. C. Agrawal, *Electrical Power Engineering: Reference Applications Handbook*. Boca Raton, FL, USA: CRC Press, 2007.
[24] *Data Sheet: PC (polycarbonate) Production-Grade Thermoplastic for FORTUS 3D Printers* Stratasys, Eden Prairie, MN, USA, 2018, pp. 3–4.
[25] J. L. Coronel, K. H. Fehr, D. D. Kelly, D. Espalin, and R. B. Wicker, "Increasing component functionality via multi-process additive manufacturing," *Proc. SPIE*, vol. 10194, p. 101941F, May 2017.
[26] E. MacDonald and R. Wicker, "Multiprocess 3D printing for increasing component functionality," *Science*, vol. 353, no. 6307, Sep. 2016, Art. no. aaf2093.
[27] *11 Standard Terminology for Additive Manufacturing—Coordinate Systems and Test Methodologies*, Standard ASTM F2921, ASTM Int., West Conshohocken, PA, USA, 2011.
[28] B. K. Gupta, G. C. Stone, and J. Stein, "Stator winding hipot (high potential) testing," in *Proc. IEEE Elect. Insul. Conf.*, May/Jun. 2009, pp. 409–413.
[29] *IEEE Standard Techniques for High-Voltage Testing*, IEEE Standard 4, 1995, pp. 1–135.
[30] W. J. Monzel, B. W. Hoff, S. S. Maestas, D. M. French, and S. C. Hayden, "Dielectric breakdown of additively manufactured polymeric materials," *IEEE Trans. Dielectrics Elect. Insul.*, vol. 22, no. 6, pp. 3543–3549, Dec. 2015.
[31] J. Torres, J. Cotelo, J. Karl, and A. P. Gordon, "Mechanical property optimization of FDM PLA in shear with multiple objectives," *Jom*, vol. 67, no. 5, pp. 1183–1193, May 2015.

KAZI MD MASUM BILLAH received the B.S. degree in mechanical engineering from the Khulna University of Engineering & Technology, Bangladesh, in 2013, and the master's degree in mechanical engineering from The University of Texas at El Paso (UTEP), in 2017. He is currently pursuing the Ph.D. degree. Since 2016, he has been a Mechanical Engineering Research Assistant with the W.M. Keck Center for 3D Innovation, UTEP. His research interests include the applications of multifunctional-multimaterial hybrid additive manufacturing, materials design, fabrication, characterization, mechanical testing, rapid prototyping, and technology development.

JOSE L. CORONEL, Jr. , received the B.S. and M.S. degrees in mechanical engineering from The University of Texas at El Paso, in 2013 and 2015, respectively. He is currently pursuing the Ph.D. degree with the W.M. Keck Center for 3D Innovation, where he was a Graduate Research Assistant, where he focused on developing the foundry multi3D system for hybrid additive manufacturing using a robot arm and also currently serves as the Research Manager. He has been involved with several projects relating to system integration and embedded electronics within printed parts.

MICHAEL C. HALBIG received the B.S. degree in physics from Illinois State University, the B.S. degree in ceramic engineering from the University of Illinois, and the M.S. degree in materials science and engineering from Case Western Reserve University. He was a Materials Engineer with the U.S. Army Research Laboratory, Cleveland, from 1995 to 2010. In 2010, he joined NASA GRC. He is currently a Materials Research Engineer with the NASA Glenn Research Center (NASA GRC), Cleveland, OH, USA. His previous research interests include the environmental durability, oxidation kinetics, oxidation inhibition, and thermal shock of carbon fibers, carbon fiber reinforced SiC composites, and ultra-high temperature ceramics. His current research interests include developing joining and integration technologies for aerospace applications and are leading a project to utilize additive manufacturing technologies to enable new electric motor designs that have higher power densities and efficiencies.

RYAN B. WICKER received the B.S. degree in mechanical engineering from The University of Texas at Austin, in 1987, the M.S. and Ph.D. degrees in mechanical engineering from Stanford University, in 1991 and 1995, respectively, and the P.E. degree. He is currently the Endowed Mr. and Mrs. MacIntosh Murchison Chair I Professor of mechanical engineering with The University of Texas at El Paso (UTEP), and the Director and the Founder of the W.M. Keck Center for 3D Innovation (Keck Center), UTEP. The Keck Center represents a world-class facility that focuses on the use and development of additive manufacturing technologies for fabricating 3D objects that are plastic, metal, ceramic, of bio-compatible materials, composite materials, or that contain electronics. Major efforts are underway at the Keck Center in the areas of additive manufacturing technology development; closed-loop process control strategies for additive manufacturing; additive manufacturing of various powder metal alloy systems; and 3D structural electronics in which electronics, and thus intelligence, are fabricated within additive manufacturing-fabricated structures. He is also an Editor-in-Chief and a Founding Editor of *Additive Manufacturing* and an Elsevier journal.

DAVID ESPALIN is currently an Assistant Professor with the Department of Mechanical Engineering, The University of Texas at El Paso. He also serves as the Director of research with the W.M. Keck Center for 3D Innovation—a multi-disciplinary center focused on the advancement and adoption of additive manufacturing (or more commonly known as 3D Printing) through activities in education, research, outreach, technology development and commercialization, and industrial partnerships. His current research interests include hybrid additive manufacturing, large area additive manufacturing, 3D electronics fabrication, and design software development.